Acta Materialia 239 (2022) 118259

Contents lists available at ScienceDirect

Acta Materialia

journal homepage: www.elsevier.com/locate/actamat

Full length article

Mechanical surface treatment studies by Bragg edge neutron imaging

Ranggi S. Ramadhan[a,b,f,1,*], Daniel Glaser[c], Hitoshi Soyama[d], Winfried Kockelmann[b], Takenao Shinohara[e], Thilo Pirling[f], Michael E. Fitzpatrick[a], Anton S. Tremsin[g]

[a] Faculty of Engineering, Environment and Computing, Coventry University, Coventry CV1 2LD, UK
[b] Science and Technology Facilities Council (STFC) Rutherford Appleton Laboratory, ISIS Facility, Harwell OX11 0QX, UK
[c] Council for Scientific and Industrial Research (CSIR), Pretoria, South Africa
[d] Department of Finemechanics, Tohoku University, Aoba 6-6-01, Aramaki, Aoba-ku, Sendai 980-8579, Japan
[e] J-PARC Center, Japan Atomic Energy Agency (JAEA), 2-4 Shirakata, Tokai, Ibaraki 319-1195, Japan
[f] Institut Laue-Langevin, 71 Avenues des Martyrs, Grenoble 38000, France
[g] Space Sciences Laboratory, University of California, Berkeley, CA 94720, USA

ARTICLE INFO

Article history:
Received 5 July 2021
Revised 11 July 2022
Accepted 7 August 2022
Available online 15 August 2022

Keywords:
Bragg edge
Neutron imaging
Surface treatment
Cavitation peening
Laser peening
Residual stress

ABSTRACT

Mechanical surface treatment technologies such as laser peening and cavitation peening require detailed characterization, including residual stress analysis, to optimize their processing parameters. Recent developments at neutron facilities allow non-destructive 2-dimensional residual strain mapping through Bragg edge imaging, which provides specific advantages over more established methods. The present work highlights the application of Bragg edge neutron imaging for the study of mechanical surface treatments, through determination of lattice spacing distributions by energy-resolved radiography. Through three different examples, the unique capabilities of the method are demonstrated, particularly for providing near surface residual strain maps within samples with complex geometries with relatively high spatial resolution. By providing a comparison with X-ray diffraction and neutron diffraction results, the present work emphasizes the potential of Bragg edge neutron imaging as a tool for surface treatment research.

1. Introduction

Improvement of mechanical and fatigue performance of engineering components can be achieved through different mechanical surface treatment methods (e.g., [1–3]). A classic example of such a method is shot peening for which controlled impingement of solid shot media (e.g., glass, metallic, or ceramic spheres) generates plastic deformation on the surface which leads to a material response in the form of compressive residual stress fields [4]. More recently, laser peening has become an attractive surface processing technology, that uses a laser-induced shockwave to generate similar effects to shot peening but with deeper compressive stress fields and better surface finish [5]. Novel peening methods such as cavitation shot-less peening that uses cavitation bubble impacts have been developed [6]. Among other beneficial effects, these treatments generate compressive residual stress near the surface of components, which counteracts the applied forces and leads to extension of service life. Since the introduction of compressive residual stress is one of the key factors in improving fatigue performance by mechanical surface treatments, the quantitative evaluation of residual stress generated by the process is integral in the design and development of these technologies.

In the past, slitting and hole drilling has been used for peening research [7,8], both of which are destructive methods. Laboratory X-ray diffraction, via the $\sin^2\psi$, $\cos\alpha$, and 2D methods [9] can be used non-destructively for surface stress measurement, but require electrochemical polishing to determine the depth-wise stress distribution. Full non-destructive methods such as synchrotron X-ray diffraction [10–12] and neutron diffraction [13,14] have been applied to resolve the full stress tensor near the surface and through the bulk of components, although they have limitations in terms of spatial resolution in one or more directions, and require many measurement points. The combination of these complementary X–ray and neutron measurement techniques has provided essential insight into residual stress profiles, e.g., within laser peened components [15].

Opportunities have arisen for neutron imaging of residual strain in engineering components [16–22], rapidly (in a few hours) and with high spatial resolution (few hundred microns), as a result of

* Corresponding author at: Solid Mechanics Research Group, Department of Mechanical Engineering, University of Bristol, Bristol, BS8 1TR, UK.
E-mail address: ranggi.ramadhan@bristol.ac.uk (R.S. Ramadhan).
[1] Present address: Solid Mechanics Research Group, Department of Mechanical Engineering, University of Bristol, Bristol, BS8 1TR, UK.

https://doi.org/10.1016/j.actamat.2022.118259

recent developments in energy-resolved imaging [23] and new detector technologies [24], as well as access to dedicated time-of-flight (TOF) neutron imaging instruments [25,26]. The technique analyses Bragg edges which refer to pronounced rises of transmission at certain wavelengths due to neutrons being removed by Bragg diffraction. The neutron wavelengths of Bragg edges relate directly to the lattice spacings of the corresponding *hkl*-planes, and the variation of these spacings across the bulk sample can be reconstructed into two-dimensional maps, which in some cases can be translated into maps of strain given a suitable reference. Relatively large strain maps across many millimeters can be obtained in a single exposure in a transmission geometry, which is a considerable advantage compared to direct scanning of diffraction signals by other non-destructive techniques (e.g., neutron and X-ray diffraction) [22]. The information is however averaged through the sample thickness and the measured strain direction is always along the incident beam direction. Consequently, the technique lends itself mainly to determine strain for one strain components, assuming that the strain does not vary along the neutron path within a sample or that an averaged value through the sample thickness is acceptable (e.g., can be interpreted using computer simulations of 3-dimensional stress distributions).

Two-dimensional strain information for one component is useful in many cases, particularly when gathered faster, easier, and with higher resolution than for complementary techniques. For example, surface strains can be studied within the spatial resolution limits of typically several hundred micrometers. Bragg edge imaging also does not suffer from the pseudo-strains problem of neutron diffraction for near-surface or near-interface strain measurement due to partial immersion of a gauge volume in a sample [27]. Meanwhile, thickness-dependant pseudo-strains were observed in Bragg edge transmission [28,29] but could not yet be fully explained. In the present work, the specific advantages and pitfalls of Bragg edge neutron imaging for surface peening research are demonstrated through the method's application in three study cases. Correlations between strain measurements by neutron imaging and more established methods are examined. The demonstration of these cases may encourage further development of Bragg edge neutron imaging as a surface analysis tool for materials and engineering research.

2. Methods and instruments

2.1. Basic concept

A Bragg edge transmission pattern is characterized by a sequence of sudden jumps as a function of neutron wavelength λ. Bragg edges occur due to coherent backscattering (Bragg angle $\theta = 90°$) of neutrons into the incoming beam direction at a critical wavelength of $\lambda = 2d_{\mathrm{hkl}}$ by a family of (hkl) planes perpendicular to the beam, assuming random grain orientations of a sufficient number of grains. Above this critical value, a corresponding (hkl) set of planes no longer contributes to the coherent scattering, hence the sudden increase in transmission. Therefore, the specific wavelength localization of a Bragg edge can be used to precisely determine the average lattice spacings of the properly oriented grains. Lattice spacing information from a carefully selected single or from multiple (hkl) planes can reflect the macroscopic mechanical behavior of a specimen under applied and/or internal stresses. Bragg edge analysis is analogous to Bragg peak analysis in diffraction measurements. Fig. 1(a) compares Bragg edges and Bragg peaks for an aluminium alloy 2024 (AA2024) powder.

Bragg edge transmission measurements require a wavelength-resolving setup, which is achieved with sufficient $\Delta\lambda/\lambda$ resolution using a polychromatic beam on a time-of-flight instrument on a pulsed neutron source [26]. Furthermore, for Bragg edge imaging

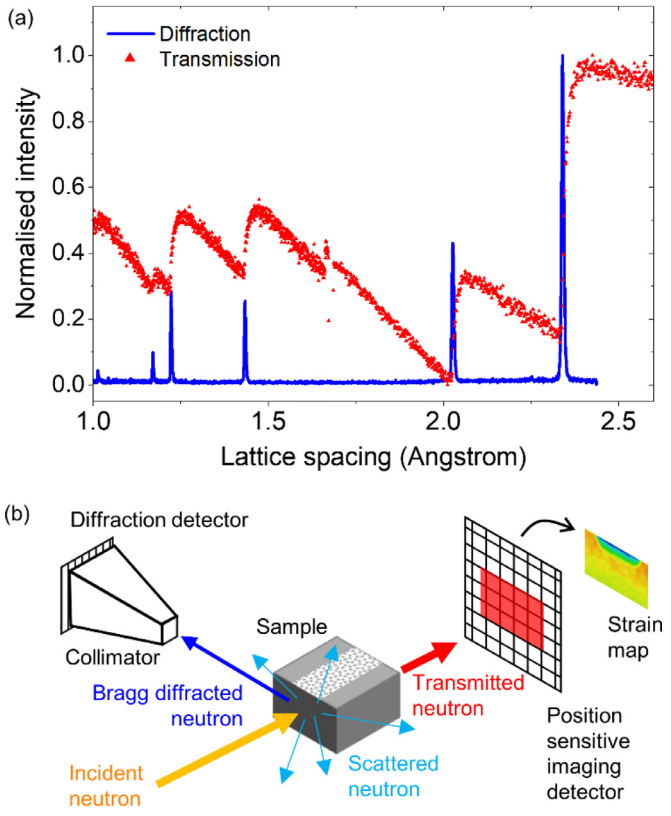

Fig. 1. (a) Diffraction and transmission spectra of AA2024, measured on ENGIN-X and IMAT [30] beamlines at ISIS, respectively. The feature in the transmission spectrum at 1.7 Angstrom is an artefact of the data collection and data processing procedures; (b) Illustration comparing neutron diffraction and Bragg edge neutron transmission setup. For neutron diffraction a pencil beam is used; for Bragg edge imaging the whole camera sensor is illuminated.

a spatial- and time-resolving neutron detector is required. Bragg edge transmission is preferably performed using a wide neutron wavelength range, extending beyond neutron wavelengths $\lambda > 2d_{hkl}$ of the lowest index (hkl) of materials which for most metal crystal structures are below 5 Å.

The sample is placed between the neutron source and the detector, Fig. 1(b), so that the spatial information is preserved. The Bragg edge information can be extracted pixel-by-pixel, therefore the physical size of the detector pixel affects the spatial resolution of the measurement. Furthermore, the temporal widths of neutron pulses (spectral component) and the divergence of the neutron beam (spatial component) contribute to the $\Delta\lambda/\lambda$ resolution. The latter is usually controlled by a collimator in the incident beam, often referred to a as a 'pinhole' or beam aperture. The size of the pinhole *D*, the distance of the pinhole from the detector *L*, and the distance between the detector and the sample *l* thus are major contributors to the spatial resolution. The wavelength-dependent effects of these parameters to the effective spectral and spatial resolution for neutron imaging were characterized elsewhere [20]. Such a pinhole setup effectively creates a low-divergent neutron beam, which is suitable for neutron Bragg edge radiography with sub-millimeter spatial resolution.

The positions of Bragg edges are determined by fitting adequate Bragg edge functions which yields high-precision d-spacings often two orders of magnitude below the $\Delta\lambda/\lambda$ instrumental resolution. Several models are available for fitting a Bragg edge and accurately determining its position [28,31–34]. From the Bragg edge positions of the sample λ_i and a stress-free reference λ_0, strain ε can be derived (Eq. (1)). Given the measurement geometry, the strain in-

formation is averaged through the thickness of the material in the beam propagation direction, with the measured strain direction being parallel to the beam. This renders the determination of 3-D stress or strain tomography through this technique improbable for general cases. While some have demonstrated the possibility for special geometries [35–37], the ill-posed problem of strain tomography has been highlighted [38]. Tomographic reconstruction of 2D strain fields, i.e. resolution of strain in the beam direction, has been demonstrated by Gregg et al. [29] by imposing equilibrium conditions at test points.

$$\varepsilon = \frac{\lambda_i - \lambda_0}{\lambda_0} \tag{1}$$

2.2. Neutron imaging instruments and detectors

Bragg edge neutron imaging is available at several large-scale research facilities around the world. This work was performed on the IMAT beamline at ISIS, UK [30,39], and on the RADEN beamline at J-PARC, Japan [25]. IMAT is installed on the ISIS second target station, which operates at 10 Hz and provides a liquid hydrogen moderator at 18 K that produces a spectrum which peaks at 2.6 Å. The flightpath of IMAT is around 56 m, with the aperture to detector distance $L = 10$ m. The beamline has a range of available pinholes, for variable settings of the beam divergence L/D. Usually, an aperture D is selected so that the geometric blur matches the targeted spatial resolution given by the pixel size of the detector and the requirements for pixel binning during the analysis (see below). The sample positioning stage of IMAT includes two perpendicular tilt alignment axes and a rotation stage.

Meanwhile, RADEN is the world's first dedicated neutron imaging instrument using pulsed neutrons, launched into operation in November 2014. It is installed at beamline number 22 (BL-22) in the Materials and Life Science Experimental Facility (MLF) of J-PARC. RADEN views the decoupled hydrogen moderator which is located at 18 m from the 'near sample position' and 23 m from the 'far sample position'. RADEN provides about four times smaller widths ($\Delta\lambda/\lambda$ ~0.2%) of neutron pulses compared to IMAT ($\Delta\lambda/\lambda$ ~0.8%) for wavelengths > 3 Å and for a similar L/D. At the time of the experiments, the neutron flux levels on both instruments, and hence the collection times, were comparable. The sharper neutron pulses, and consequently sharper Bragg edges, are a characteristic feature of RADEN which is relevant if high strain resolution and separation of overlapping Bragg edges is required. Beam optics comprises a heavy shutter, two rotary collimators, and beam slits that are installed to provide various L/D values and beam sizes. For the case study in this work, the samples were mounted on the medium sample stage at the near sample position (flightpath of 18 m). An aperture with $D = 50.1$ mm, which is placed 3.1 m from the source, was used. The proton beam power was 500 kW at the time of experiments.

For the present work, micro-channel plate (MCP)/Timepix imaging detectors [24] were installed and used on the two instruments. The detector has 512 × 512 pixels, each with 55 µm size, providing 28 × 28 mm^2 of active area. The detector was synchronized to the neutron source for the time-of-flight measurements. The time-of-flight range for the measurements was chosen to cover several Bragg edges of a sample, with corresponding wavelengths between 1 and 5 Å. About 3000 time bins were used, with time bin widths between 20 and 40 µs depending on the given spectral resolution functions of the two instruments IMAT and RADEN. For each time channel a quasi-monochromatic radiograph was obtained, and thus each data collection yielded a stack of up to 3000 radiographies. In other words, each TimePix chip pixel provided a Bragg edge spectrum with up to 3000 wavelength channels.

3. Samples, surface treatments and measurement details

3.1. Study cases

Different aspects of peening research, i.e., peening methods, peened surface geometry, and peening coverage were studied in this work. Three different materials were investigated, namely JIS SKD61 ferritic steel, 12%Cr martensitic stainless steel, and aluminium AA7050. The chemical composition of each material can be found in Table 1.

The first case study concerns the effect of different peening methods of JIS SKD61 steel samples: water jet-accelerated shot peening, submerged laser peening, and cavitation peening, all without applying sacrificial/ ablation layer on the treated surface. Schematics showing the mechanism of each peening method is presented in Fig. 2. Naito et al. [40] developed a shot peening system accelerated by a water jet, Fig. 2(a), where shots, i.e., 500 3.2 mm diameter steel balls were accelerated and circulated by water jet and impinging a specimen surface. The study shown generated residual stress distributions similar to those from conventional shot peening. The development aimed to reduce the risk of dust explosions and health hazards which was reported for conventional shot peening [41]. Submerged laser peening, Fig. 2(b), produces peening impacts from both the plasma generated by the laser ablation of the sacrificial layer and the collapse of cavitation bubbles generated after laser ablation. Elevated compressive in-plane residual stress can be achieved in the sub-surface, but tensile stress out-of-plane stresses on the surface may be present depending on the use of sacrificial layer [42]. In cavitation peening, Fig. 2(c), a component's surface is peened by cavitation impacts generated by a submerged high-speed water jet, i.e., a cavitating jet. It has been employed for several applications [43,44] and can be used to peen relatively hard steel [45]. Since the mechanism of the impact force differs depending on the peening method, it was worthwhile to investigate the introduced compressive residual stress for each peening technique.

The size of the specimens used for Bragg edge neutron imaging and X-ray diffraction was 15 mm × 15 mm × 6 mm. To examine the effect of the peening methods on the introduced residual strain or stress under the same conditions, the peening intensity of each peening method was evaluated using the arc height of the Almen strip. An Almen strip is commonly used to quantify the intensity of a peeing process, where the peening intensity is correlated with the deflected arc height in the Almen strip processed with the same parameters [46]. A Type A Almen strip was used in the present experiment. The arc height was measured using a standard-compliant test strip gauge. The change in the arc height $h_A = 0.2$ mm was used as the common intensity unit for the different peening methods, which corresponds to a specific peening intensity value for each method ($t_p = 0.167$ s/mm for shot peening, $t_p = 10$ s/mm for cavitation peening, and $d_L = 5$ pulse/mm^2 for laser peening). Three peening intensities (low, medium, and high) were applied using each peening method, giving a total of nine treated specimens and one non-treated sample (see Fig. 3(a) and Table 2).

The second study case was on the application of laser peening on complex geometries. Laser peening has been proposed to improve the fatigue life of highly stressed turbine blade components for power generation purposes, specifically the fir-tree root of the turbine blade, see Fig. 3(c). While shot peening is commonly used for this application, there are some concerns over the effectiveness of that process, especially after a catastrophic failure of one of these blades at a South African power station, resulting in loss of production and considerable financial damages. Residual stress measurement in a typical blade attachment profile has been a challenge due to the complex shape and nature of the material.

Table 1
Chemical compositions of the tested sample materials (mass%).

	C	Si	Mn	P	S	Cu	Ni	Cr	Mo	V
JIS SKD61	0.38	0.95	0.43	0.023	0.03	0.11	0.15	5.30	1.22	0.80
12Cr SS	0.08–0.15	0.17–0.37	0.40–0.70	–	–	–	–	0.30–0.60	0.25–0.35	0.15–0.30
	Fe	Si	Mn	Mg	Zn	Cu	Zr	Cr	Ti	Others
AA7050	max. 0.15	max. 0.12	max. 0.1	1.9–2.6	5.7–6.7	2.0–2.6	0.08–0.115	max. 0.04	max 0.06	0.05–0.15

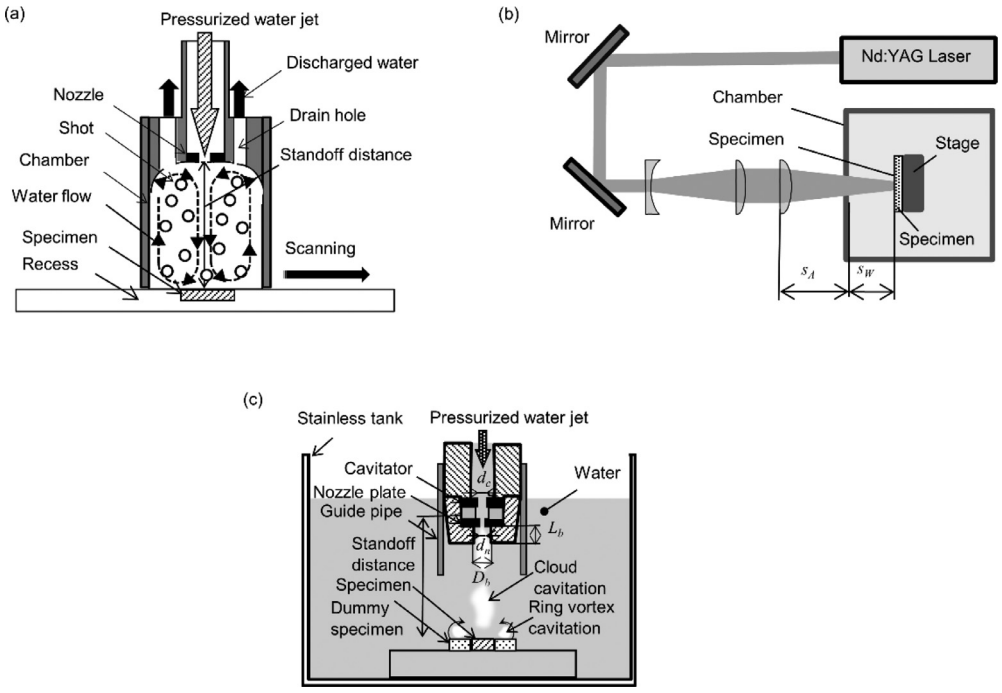

Fig. 2. Schematics showing the mechanism of different surface peening techniques: (a) water jet-accelerated shot peening, (b) laser shock peening, and (c) cavitation shotless peening.

Table 2
Summary of the processing time per unit length or pulse density for the residual strain and stress measurements of JIS SKD61 samples.

Peening intensity Unit t_p or d_L (h_A = 0.2 mm)	Peening method		
	Shot peening (SP) t_p = 0.167 s/mm	Cavitation peening (CP) t_p = 10 s/mm	Laser peening (LP) d_L = 5 pulse/mm^2
Low (× 2)	t_p = 0.333 s/mm (**SP-LOW**)	t_p = 20 s/mm (**CP-LOW**)	d_L = 10 pulse/mm^2 (**LP-LOW**)
Medium (× 4)	t_p = 0.667 s/mm (**SP-MED**)	t_p = 40 s/mm (**CP-MED**)	d_L = 20 pulse/mm^2 (**LP-MED**)
High (× 8)	t_p = 1.333 s/mm (**SP-HIGH**)	t_p = 80 s/mm (**CP-HIGH**)	d_L = 40 pulse/mm^2 (**LP-HIGH**)

In this study, measurements were performed on test specimens representing complex-shaped fir tree samples. Three coupons made of 12%Cr martensitic stainless steel commonly used in steam turbine blade applications, were prepared. The coupons were especially manufactured and peened to resemble the peening process on a fir-tree shaped turbine blade root containing convex and concave features. Samples T1-convex and T2-concave are square-shaped coupons having a width of 20 mm and a thickness of 10 mm, with corners machined to have a convex and concave shapes, respectively. Laser peening was applied on two corners of the samples, see Fig. 3(d). The peening was carried out by the CSIR National Laser Centre, South Africa, using a peening system with peen spot size of 0.6 mm, peening coverage of 60 peen spot per mm^2, and a peening intensity of 5–6 GW/cm^2. Sample T3-groove has dimensions of 20 mm × 20 mm × 15 mm. For sample T3-groove, a half-round groove with a radius of 2.5 mm was machined on the top surface of the sample, Fig. 3(d). Laser peening was applied to the top surface, including the half-round groove and some part of the flat surface, using an upgraded peening system with a peen spot size of 0.8 mm, peening coverage of 60 peen spots per mm^2, and peening intensity of 11–12 GW/cm^2.

The third study comprised five aluminium blocks made of 7050 aluminium. The samples have dimensions of 75 mm × 17 mm × 15 mm and are offcuts from an actual wingtip device or 'winglet' of an aircraft. The purpose of this measurement was to study the residual strain in samples, which are peened with high peening intensity and coverage. Such parameters were experimentally applied to compensate undesirable bending of aircraft structures while also introducing beneficial residual stresses. Four samples were peened on one side with the width of the peened area of 10 mm along the length of a sample, Fig. 3(f). The peening was carried out by CSIR National Laser Centre, South

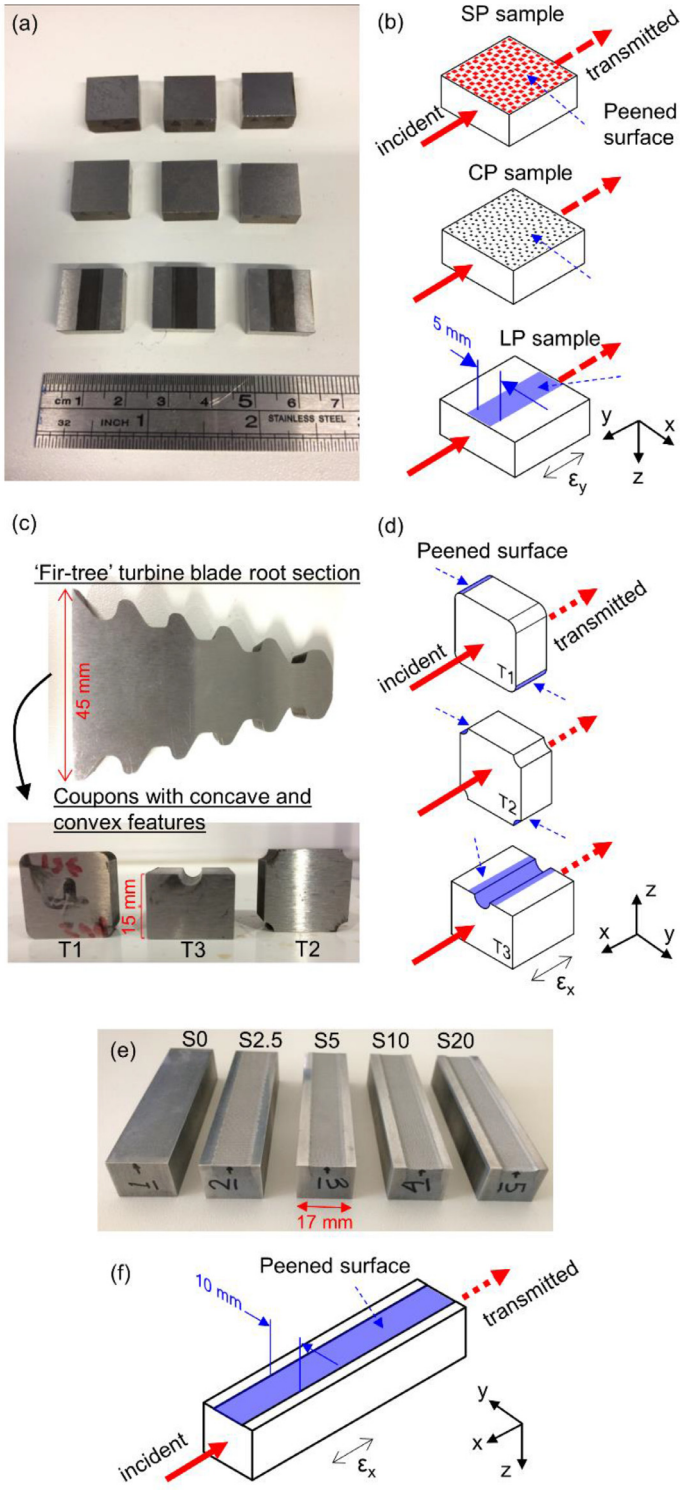

Fig. 3. Photos and schematics of the Bragg edge neutron transmission measurements on (a) and (b) JIS SKD61 tool steel specimens; (c) and (d) 12% Cr stainless steel specimens, and; (e) and (f) AA7050 specimens. Incident beam from the neutron source and transmitted beam directions into the transmission detector are indicated by red arrows. The measured strain components are parallel to the transmission direction and indicated in the schematics.

Africa, using a circular peen spot with diameter of ~1.45 mm, power intensity of ~11.1 GW/cm^2, and pulse duration of ~5 ns. The peening coverage for different samples was varied with values of 2.5, 5, 10 and 20 spots per mm^2 for samples S2.5, S5, S10, and S20, respectively. Sample S0 was not peened and was used as the reference.

3.2. Measurement details

Bragg edge neutron imaging was applied alongside more established stress determination methods. Using Bragg edge imaging, each sample was aligned in front of the detector, visually using a laser pencil beam and then followed by fine-tuning of the sample orientation using neutron radiography scans. Accurate sample alignment was essential with regard to averaging of parameters along the beam direction and direction uncertainty of the measured strain component. For all samples in this study, the measured strain is parallel with one of the sample edges (see Fig. 3). Thus, angular alignment in two directions using neutron radiograms aimed at minimizing the blur of the sample edges, so that the front face of the sample was as perpendicular to the main beam direction as possible. For the Bragg edge image collections, the sample was positioned close to the detector to minimize the geometric blur due to the divergent beam. Detector readout times and channel widths were configured for a given material. The data collection times varied between 2 and 8 h. For each detector setting (different shutter settings determining which part of transmission spectra is not measured due to detector readout deadtime), an 'open beam' data set was collected, with the sample removed.

For the JIS SKD61 tool steel samples, the residual strain in the peened surface was measured by Bragg edge neutron imaging, while the residual stress was measured by X-ray diffraction using the 2D XRD method, and the results from both techniques were compared. Bragg edge neutron imaging was performed on the IMAT beamline at ISIS, UK, using a pinhole size D = 40 mm (L/D = 250). The samples were placed between the neutron source and the detector, where the distance between the middle of the sample and the neutron-sensitive MCP of the detector was l ~35 mm. Three specimens were measured at once in one exposure, with a counting time of 8 h for the treated specimens. The counting time was halved for the non-treated specimen due to limited beam time. The measured strain component is illustrated in Fig. 3(b).

X-ray diffraction was carried out on a duplicate sample set. The 2D XRD method was used, since it was shown to provide good accuracy for investigation of peened specimens [42]. CrKα radiation was used at 35 kV and 40 mA. The diameter of the collimator was 0.8 mm, and the diffraction from a 4 × 4 mm^2 area on the surface was obtained by moving the specimen perpendicularly to the X-rays. The α-Fe(211) plane was used for the measurement at a diffraction angle of 156°. Twenty-four diffraction rings from the specimen at various angles were detected, for an exposure time of 20 s per frame at each position. To determine the change in the distribution of the residual stress with the depth from the surface, electrochemical polishing was used.

12%Cr SS complex geometry coupons were measured on IMAT using D = 80 mm (L/D = 125). The samples were placed between the neutron source and the detector, with middle of sample-to-detector distance of l ~35–40 mm. The counting time for each sample was 4 h, and the direction of the measured strain component is illustrated in Fig. 3(d). Neutron diffraction measurement was also performed on the sample T3-groove on the SALSA beamline, ILL [47]. A scan was performed vertically along the radius of the groove (see later Fig. 7(a)), using a gauge volume of 0.6 mm vertically and 2 mm horizontally. Using the incident beam wavelength of 1.67 Å, the detector was positioned at 2θ = 47° to measure the Fe(110) reflection. To measure the near-surface residual strain profile, an entry-scan procedure (i.e., gradual immersion of GV into the sample and correcting pseudo-strain with separate calibration measurement) [48] was performed. 43 points were measured with a total counting time of 3.5 h for one strain component.

For the AA7050, Bragg edge neutron imaging measurements were performed on the RADEN beamline. An aperture of

D = 50.1 mm and L = 18 – 3.1 m, thus L/D ratio of ~298 was used, with middle of sample-to-detector distance of l ~60 mm. The direction of the measured strain component is indicated in Fig. 3(f), while the counting time for each measurement was 4 h, with two samples measured in each exposure.

3.3. Data analysis

A Bragg edge fitting function described in [31,33] was used in this study (Eq. (2)). While pixel-by-pixel analysis is possible in principle, strain maps were reconstructed from Bragg edge information averaged from a combination of a group of pixels, a so-called macro-pixel [49]. The running average of the macro-pixel with step size of 1 pixel (55 µm) was then applied across the image to reconstruct the strain map. This is performed to improve the statistics (and thus decreases the counting time) at the expense of spatial resolution [20]. The Bragg edge fitting and the reconstruction of Bragg edge parameter maps, i.e., edge position, height, shape, and corresponding uncertainties, were performed using *TPX_EdgeFit* (Anton Tremsin, personal communication, 1 October 2016). For the cases in this study, three Bragg edge parameters, i.e., position, edge pedestal, and edge height were fitted for the sake of robust fits of a multitude of spectra. The edge widths were fixed to values from calibration data as there was no indication of Bragg edge broadening, and as fitting the width parameter did not significantly affect the strain results. An exception was made for the data analysis of AA7050, where the edge width parameter σ was also fitted to observe plasticity. The (hkl) used for the analysis was Fe(110) for JIS SKD61 steel and 12%Cr steel, and Al(111) for AA7050. Post processing of the maps, e.g., from edge position to strain, adjusting scales and applying color maps, was performed using *Fiji* [50], a distribution of the open-source image analysis software *ImageJ*.

$$T(\lambda) = C_1 + C_2\left[\mathrm{erfc}\left(\frac{\lambda_i - \lambda}{\sqrt{2}\sigma}\right) - \exp\left(\frac{\lambda_i - \lambda}{\tau} + \frac{\sigma^2}{2\tau^2}\right) * \mathrm{erfc}\left(\frac{\lambda_i - \lambda}{\sqrt{2}\sigma} + \frac{\sigma}{\sqrt{2}\tau}\right)\right] \quad (2)$$

Fig. 4(a) shows selected Bragg edge transmission spectra exhibited by the materials of the test specimens, i.e., tool steel JIS SKD61, aerospace-grade AA7050, and 12%Cr stainless steel, taken from the specimen area equivalent to a macro-pixel size of 30 × 30. The transmission profiles and the transmission levels reflect the attenuations of the materials as well as the thicknesses of the samples. A modulation of a Bragg edge spectrum by texture is often clearly visible by comparison with the expected spectrum for randomly oriented grains, however extraction of the texture is not possible from such curves in general. The shape of the transmission spectra and Bragg edges of 12%Cr steel indicate randomly oriented grains. Meanwhile, those from the JIS SKD61 and the AA7050 specimens show the presence of crystallographic texture where ratios of Bragg edge heights deviate from the ones for randomly oriented grains, indicated by the relatively strong Fe(110) and Al(111) Bragg edges, respectively. Larger gradient and deviation from linear transmission slopes for wavelengths lower than the actual Bragg cut-off can also be observed. Fig. 4(b) and (c) highlight these Fe(110) and Al(111) edges in more detail while also showing the fitted model curves (Eq. (2)) and the Bragg-edge positions.

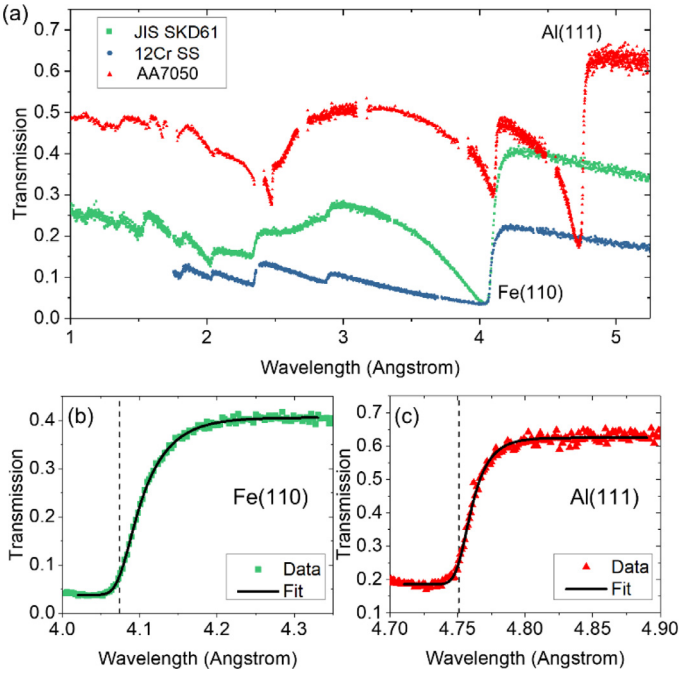

Fig. 4. (a) Selected transmission spectra of the samples studied in this work plotted for regions of interest of 30 × 30 pixels; (b) Fe(110) and (c) Al(111) Bragg edges from JIS SKD61 and AA7050 samples, respectively, fitted with Eq. (2) [31,33], where the fitted models are shown by the black solid lines. The Bragg edge positions are indicated by the dotted lines.

4. Results and discussion

4.1. Comparison of peening techniques

Fig. 5(b)–(d) show the reconstructed 2D strain maps and the line profiles of strains extracted from the corresponding maps and from the XRD measurement of the JIS SKD61 samples treated with different peening methods. A non-treated sample is also presented for comparison Fig. 5(a). The scale, sample orientation, and color bar indicative of the strain values applied for all maps are given in Fig. 5(a). The strain maps were reconstructed from Fe(110) Bragg edges using a macro-pixel size of 3 × 3 pixels (0.165 × 0.165 mm^2); in comparison, the geometric blur given by L/D and sample-to-detector distance (l) is around 140 µm. Referring to a previous characterization [20], the two parameters yield a lower limit for the achieved spatial resolution of about 150 µm. The measured strains ε_y were averaged through the sample thickness in the y-axis direction. From the XRD measurement, the region around between 700 and 1000 µm below the surface was shown to be stress-free. Therefore, the Bragg edge positions from the corresponding region of each sample was averaged and used as the d_0 reference for strain calculation.

The strain maps of the treated specimens show in-plane compressive strains indicated by the dark blue area on the top surface, which gradually diminishes further away from the surface. This contrasts with the non-treated (NP) sample, where no such area is observed. Visual inspection of the strain map can easily inform the homogeneity of the compressive residual strains generated by the peening processes. For example, the laser peened region with a width of ~5 mm is immediately visible as a region of compressive strain surrounded by unstrained, untreated region, Fig. 5(c). Strain maps of cavitation-peened samples (CP) show an increase of compressive residual stresses in both magnitudes and penetration depths as a function of peening intensity, Fig. 5(d).

To facilitate quantitative assessment and comparison, strain profiles were extracted from areas of the strain map indicated by the red-dotted line. As the XRD method provides in-plane residual stresses, strains were calculated assuming the out-of-plane stress to be zero (plane stress assumption), and ε_y were provided for comparison. In general, the strain plots show a fairly good agreement between Bragg edge imaging and XRD.

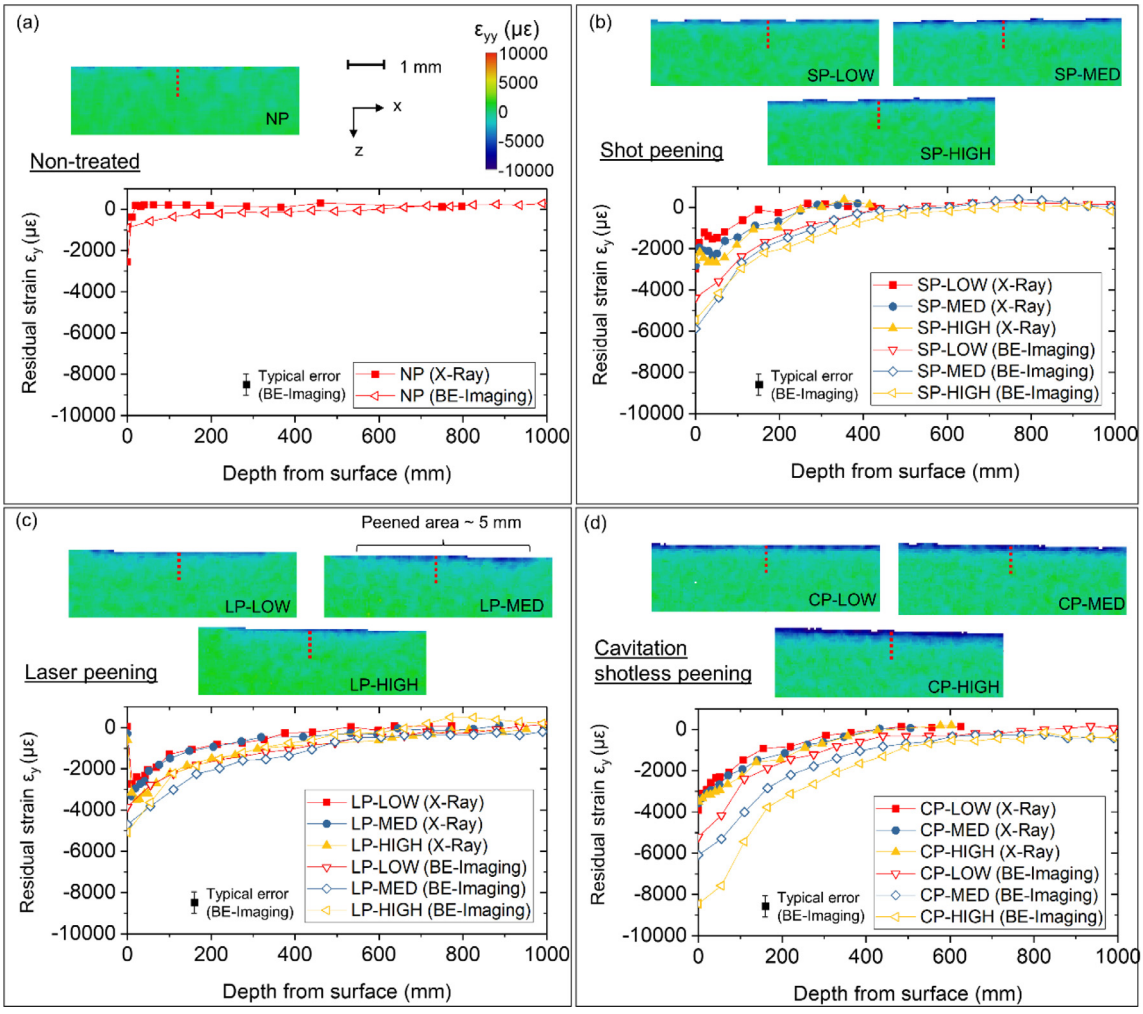

Fig. 5. Strain maps collected on IMAT and line profile of strains extracted from the map vs X-ray diffraction results, for (a) untreated, (b) shot peened, (c) laser peened, and (d) cavitation peened JIS SKD61 samples. The measured strain components are parallel to the y-axis, ε_y. The red-dotted lines on the maps indicate the locations of the plotted strain profiles. The dimensional scale, the sample coordinate axes, and the color scale are indicated in (a), which are applied for all maps. Note that the strain values are plotted in steps of the MCP pixel size of 55 µm.

For the non-treated sample (NP), Bragg edge imaging provided maximum compressive residual strain of around −900 µε, gradually diminishing and reaching zero strain at a depth of ∼600 µm from the surface while XRD showed a much higher compressive residual strain values of around −2500 µε, albeit diminishing with a steeper gradient and reaching zero strain within the first 20 µm, Fig. 5(a). The presence of compressive residual strains in the non-treated sample are expected to be generated by the grinding process, which was applied to the base material. For the shot-peened samples (SP), Bragg edge imaging and XRD results show similar trends, where the higher peening intensities (SP-MED and SP-HIGH, blue and yellow points) exhibit significantly higher compressive strain values near the surface compared to the lowest peening intensity (SP-LOW, red points), Fig. 5(b). However, the XRD results are in average around 2000 µε less compressive than Bragg edge imaging result and reach zero strain faster (at depth of around 300 µm vs. around 600 µm for Bragg edge imaging). For laser-peened samples (LP), XRD results show low compressive strain values on the surface followed by maximum compressive strains on the subsurface within the first 20 µm before gradually diminishing towards zero strain. Bragg edge imaging results do not exhibit such behavior, where the compressive residual strains were found on the sample surface.

Meanwhile, both Bragg edge imaging and XRD results agrees that cavitation peening generated the highest compressive residual strain values and deepest penetration depths among other methods. This trend corresponds well with results reported previously [6] and might have been caused by two reasons. Cavitation impact measured with a PVDF sensor [51] introduced small and large impacts at the same time. This mimics multiple stage peening, i.e., shot peening with large shots followed by small shots. The large shots introduce compressive residual stress in deeper regions, while small shots introduced large compressive residual stress near the surface. The other reason is the pressure distribution of the individual cavitation impact [52]. That said, XRD results showed significantly lower compressive strains and reached zero strain faster compared to Bragg edge imaging results.

The discrepancies between Bragg edge imaging and XRD results can possibly be explained in different ways. Firstly, while the peening methods and parameters were identical, different sample sets were used for the two experiments, therefore providing challenges for a one-to-one comparison. Secondly, the analysis from the two techniques yields different lattice strains: X-ray diffraction measured ε-Fe(211) while strain maps from Bragg edge imaging were reconstructed from Fe(110) (as the statistics of the Fe(211) Bragg edges were not sufficient for high-resolution strain mapping, which

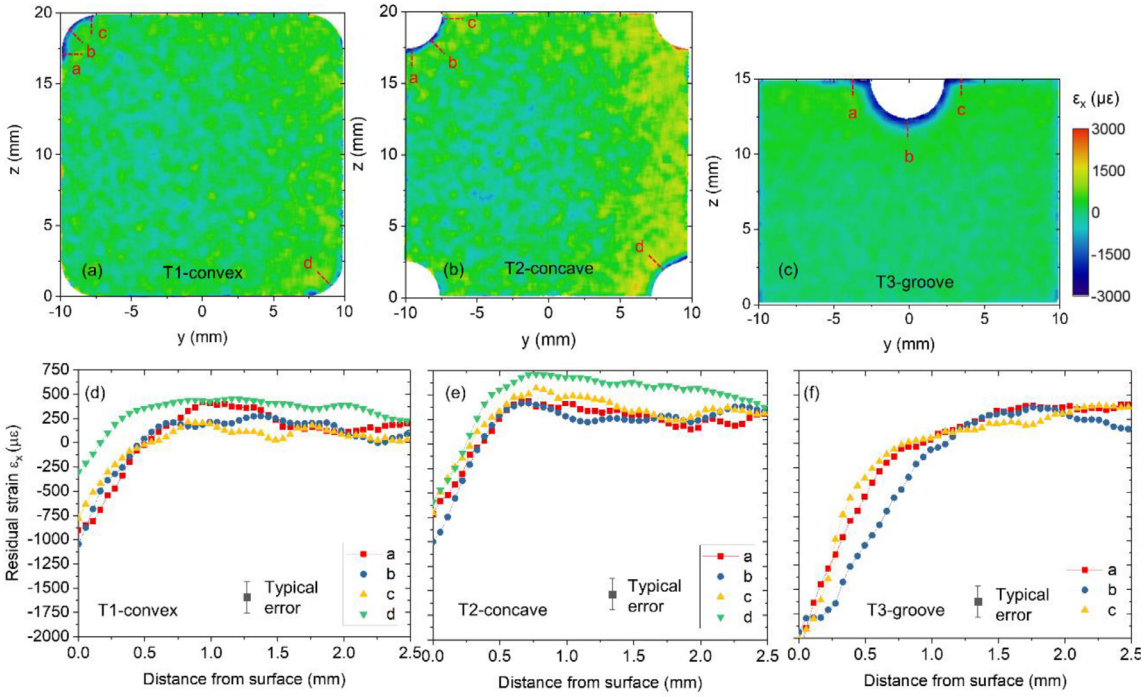

Fig. 6. Strain maps of the complex-shaped laser peened 12%Cr steel samples from IMAT, and the line profiles of strains taken from the maps (indicated by the red dotted lines).

is emphasized in this work). Bragg edge strain imaging analysis also suffers an averaging both laterally and through-the-thickness, which is another possible source of the observed discrepancies. Nevertheless, the relationship between X-ray diffraction and neutron imaging results is generally satisfactory.

4.2. Peening of complex geometries surfaces

Fig. 6 shows the reconstructed strain maps of the complex-shaped, laser-peened steel 12%Cr SS samples, reconstructed from the Fe(110) Bragg edges using a macro-pixel size of 10 × 10 pixels, averaged through the thickness in *x*-axis direction. A region in the middle of each sample was assumed to be stress-free and therefore was taken as reference (also the case for the neutron diffraction measurement). Compressive residual strain could be observed below the concave and convex laser peened surfaces. From the strain maps, the inhomogeneity of the residual strain profiles below the peened surface is immediately visible. For example, for both samples T1-convex and T2-concave, treated areas on one side, i.e., top left in Fig. 6(a) and (b), are found with higher compressive strains compared to the treated surfaces on the opposite side (bottom right). This is further indicated by the line profiles of strains taken from the 2D strain maps, as indicated by the red dotted lines, Fig. 6(d)-(e). Factoring previous evidences, these differences are presumed to originate from performance inconsistencies of the laser peening system. For the two samples, the maximum compressive residual strain was observed at the surface with values around −1000 με, and the depth of the compressive strain region is around 300–500 μm. Sample T3-groove, which was peened using different peening conditions has a deeper compressive strain up to a depth of about 500–1000 μm and a maximum compressive residual strain of about −2000 με on the surface, Fig. 6(f). The strain profile in the centre of the peened concave surface (line b) shows deeper compressive residual strains compared to the peened flat surfaces (lines a and c).

Fig. 7(b) shows reasonable agreement between neutron diffraction and neutron imaging results in measuring residual strains be-

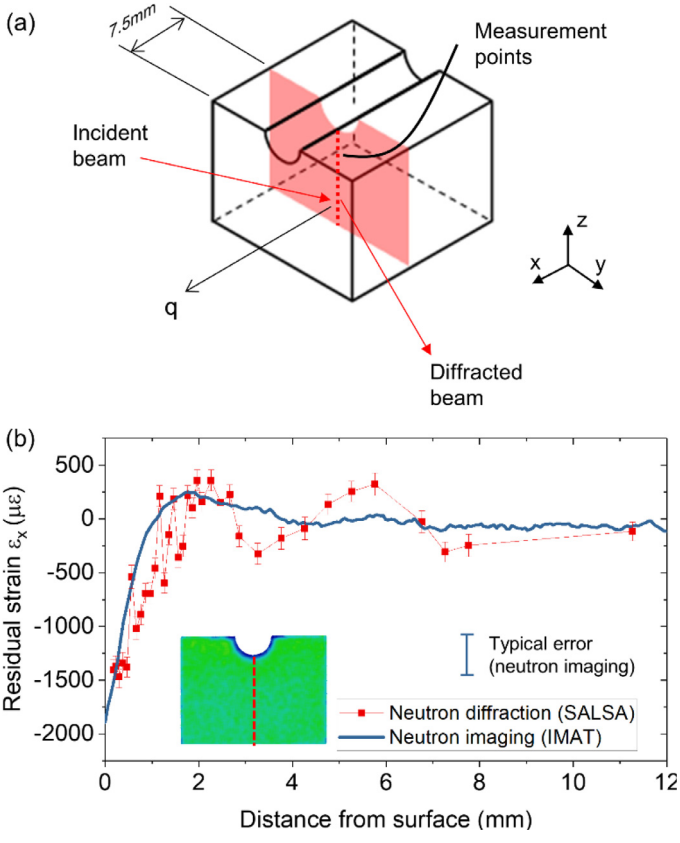

Fig. 7. (a) Illustration of the neutron diffraction setup for sample T3-groove, for which the ε_x component was measured; (b) Comparison between residual strains measured by neutron diffraction (SALSA) and neutron imaging (IMAT), both measurements using the Fe(110) reflection. The red dashed line on the map indicates the location of the plotted strain profile.

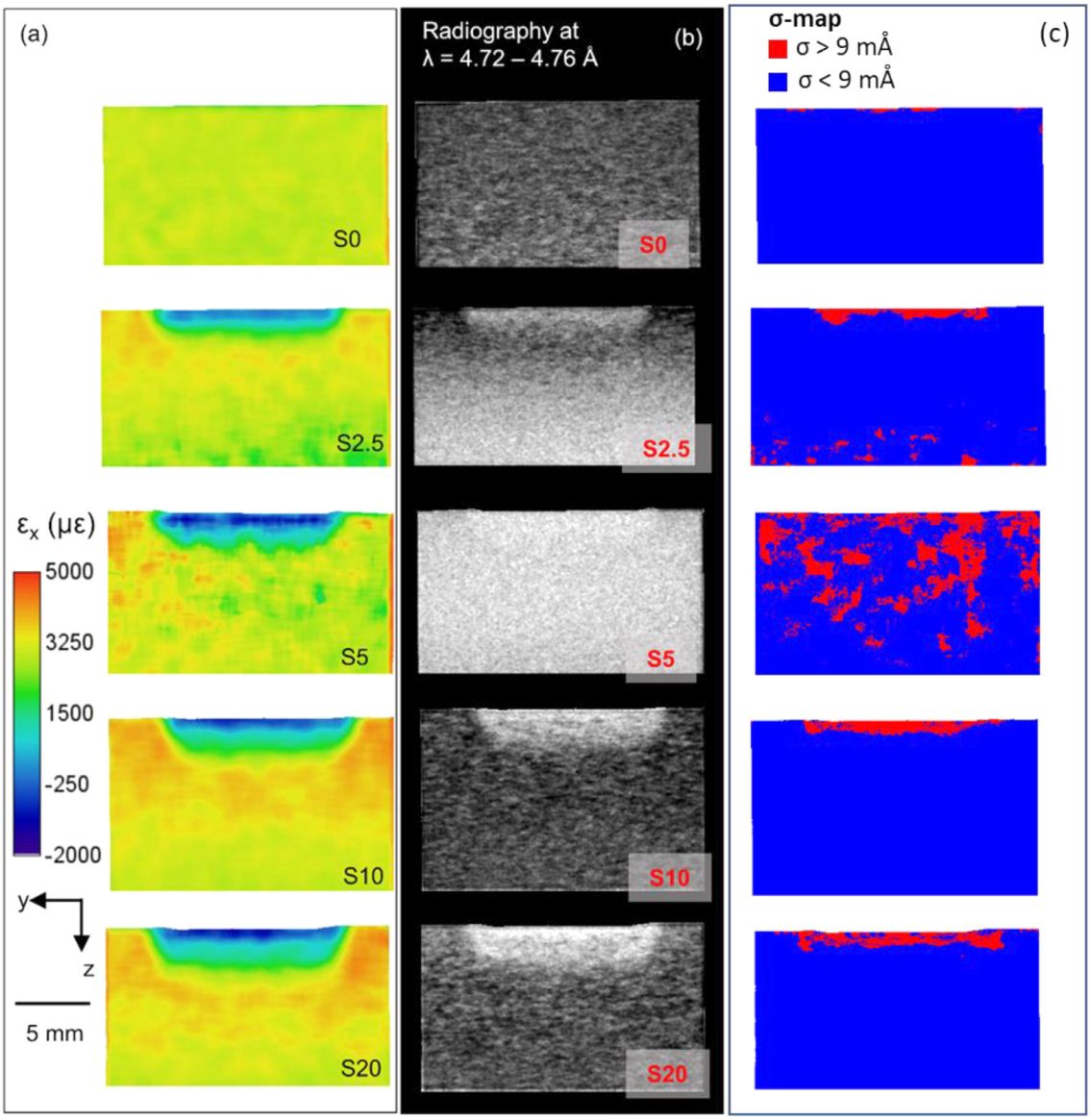

Fig. 8. (a) Strain maps of the laser peened AA7050 blocks; (b) energy-resolved radiographs extracted from the data stacks for the neutron wavelength range of 4.72–4.76 Å. The radiographs collected on RADEN are displayed over the same contrast level, with lighter colors indicating higher transmission. Significant difference in transmission is observed, especially for S2.5 and S5 compared to the rest, most likely due to crystallographic texture. Higher transmission is observed below the peened surface.; (c) σ-parameter map, with threshold of 9 mÅ applied to indicate region of plastic deformation.

low the peened area of the T3-groove sample. Both methods used the Fe(110) reflection to determine the residual strain. The near-surface measurement by neutron diffraction was only made possible by the high-flux-low-background neutron beam on the SALSA beamline, enabling the use of a comparatively small gauge size (0.6 mm). Slight discrepancies between the results are acceptable since the two methods average the strains from different gauge volumes. The effective spatial resolution of Bragg edge imaging in this case is around 300 µm. In comparison, neutron diffraction provided a spatial resolution of 600 µm in the bulk but higher towards the surface due to the entry-scan method [48]. This might explain the better agreement of the strain values close to the surface compared to the bulk.

4.3. Laser peening coverage of aluminium alloys

Residual strain maps of the AA7050 blocks are displayed in Fig. 8(a), reconstructed from the Al(111) Bragg edges using a macro-pixel size of 30 × 30 pixels for a running average of 55 µm. The area in the middle thickness of each sample was averaged and taken as stress-free reference. Compressive residual strain is observed below the peened surfaces of the samples S2.5, S5, S10 and S20, in contrast to the strain profile of the unpeened base material S0. More detailed information was obtained by plotting line profiles of strain from each of the 2D maps, Fig. 9(a). The maximum compressive strain increases with the peening coverage. Samples S2.5 (2.5 spots/mm^2) and S5 (5 spots/mm^2) have compressive residual strains at the surface of around –3000 µε. A maximum compressive strain with a value of around –3500 µε can be found at a depth of 500 µm from the surface of sample S5. Higher compressive residual strains were observed on the surface of samples with higher peening coverage, i.e., around –3900 and –4200 µε for sample S10 (10 spots/mm^2) and S20 (20 spots/mm^2), respectively, Fig. 9(a).

Further to extracting strain profiles along any line from the maps, the collected MCP image stack allows selecting radiograms for any wavelength band, as demonstrated in Fig. 8(b). Inspecting energy-selective radiograms without data processing in the wave-

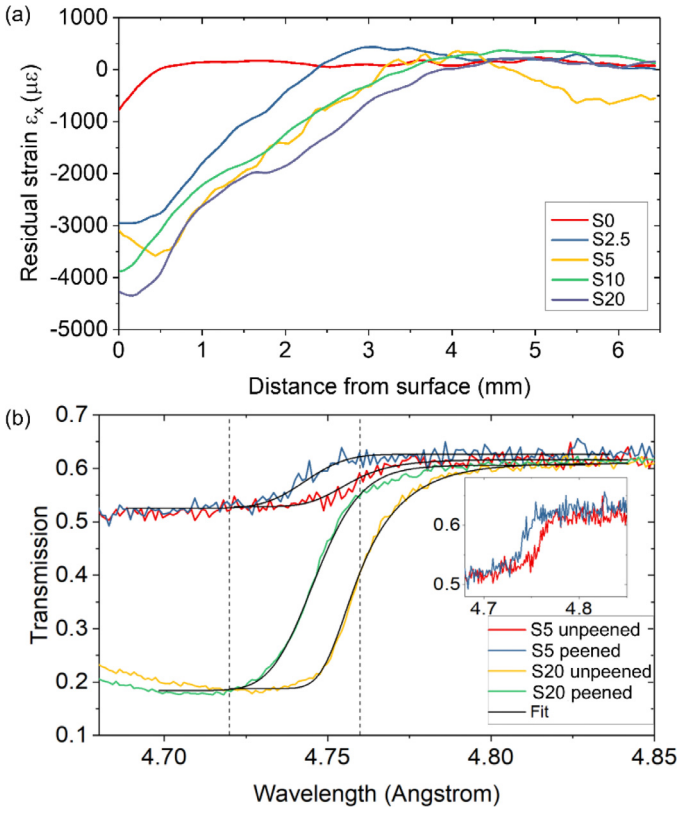

Fig. 9. (a) Line profiles of strains taken from the surface of sample S0 and peened region of sample S2.5, S5, S10 and S20; (b) Transmission spectra of peened and unpeened surfaces, taken from sample S5 (also see inset) and S20. The dotted lines indicate the lower and higher side of the wavelength range used for the energy-selective radiographs in Fig. 8(b). The significant difference in Bragg edge shapes between the samples indicates different texture, likely due to the samples taken from different section of the original offcuts.

length range of 4.72–4.76 Å (i.e., a range encompassing the Al(111) Bragg edge of AA7050) higher transmission is observed below the peened surfaces, Fig. 8(b), albeit to a much lesser degree for sample S5 (see explanation below). A detailed investigation of the transmission spectra showed that the change in contrast in the peened region is due to a significant shift of the Al(111) Bragg edge position due to the peening, combined with the low transmission at wavelengths smaller than the Bragg edge position which is caused by the long neutron paths through the sample. This leads to a significant difference in transmission near Bragg edges of peened and unpeened regions of sample S20, particularly in the wavelength range of 4.72–4.76 Å (see dotted lines in Fig. 9(b)). This effect is less obvious for sample S5, for which the height of the Al(111) Bragg edges is strongly reduced, likely due to pre-existing crystallographic texture (i.e., the crystals were aligned to a particular preferred orientation and coincidentally allowing more neutrons with the corresponding wavelength passing through), see inset in Fig. 9(b). This crystallographic texture variation along the height of the sample can also be observed in the bottom half of S2.5, Fig. 8(b).

Finally, Fig. 8(c) presents maps of the σ-parameter (Eq. (2)), which describes the Bragg edge width. The broadening of a Bragg edge (larger σ-values) can be traced back to the wider distribution of d-spacing values from each grain family, in this case due to intergranular/ type-II strain induced by plastic deformation. Therefore the σ-parameter has been used to represent regions of plasticity within a sample [53,54]. In Fig. 8(c), a threshold of 9 mÅ was obtained by calibrating the value against the non-peened sample S0, where no plasticity is expected. The threshold is then applied to all samples. A region of plasticity, indicated by the red zone, is clearly seen under the peened area of sample S2.5, S10 and S20. This matches with the visual observation of the samples (see Fig. 3(f)). A noisy σ-map, however, can be observed for sample S5 and the lower portion of S2.5. This is due to the effect of crystallographic texture significantly changing the Bragg edge shape, thus changing the σ-parameter and preventing the map to provide relevant information for the corresponding samples.

The results show that, for some cases, the effect of laser peening on the materials can be highlighted simply using energy-selective Bragg edge raw image data with minimum data processing. The contrast of transmission between the treated and non-treated areas is usually caused by the change in the lattice spacing and/or crystallographic texture in the material due to the surface treatment and can provide information about the coverage of the laser peening process. Precise determination of Bragg edge parameters such as position or width, however, is required to accurately quantify the effect of surface treatment in terms of induced residual strain or crystallographic texture. The results also indicate that the samples have different initial crystallographic textures (e.g., Sample S2.5 and S5 compared to the other three samples), most likely because the samples were taken from different section (thickness-wise) of the wing tip offcuts. This consequently leads to the samples producing slightly different Bragg edge shapes, which presents a challenge for the Bragg edge fitting analysis. In this case in particular, the presence of crystallographic texture significantly reduces the Bragg edge intensity, thus lowering the signal-to-noise ratio and reducing the precision (higher uncertainty) of Bragg edge position determination. However, the results indicate that the accuracy of the Bragg edge position is in this case preserved, as shown by the discrepancies of ~300 με between the unpeened area of S5 (textured) and S20 (non-textured), and fitted Bragg edges shown in Fig. 9(b). Therefore, the strain information can be recovered, and a strain map can still be reconstructed. That said, future work will be carried out to investigate in what cases and how texture does affect the strain measurement.

5. Discussion

Bragg edge imaging presented in this work revealed compressive residual stresses generated by the different types of peening methods. Previous studies have shown the correlation between these compressive residual stresses with the improvement of fatigue life. For example, Soyama et al. [55] showed cavitation peening improved fatigue strength of welded JIS SKD61, while Glaser et al. [56] demonstrated the improvement of fatigue life of laser-shock peened aluminium alloy for airframe application. Both studies used peening methods and materials which are presented in this work.

More advanced forms of peening require specific consideration for the target geometry. For LSP, the laser angle of incidence may affect performance, as well as the application of the inertial confinement overlay (water) applied over the surface. For CP the surface geometric features may affect the hydrodynamic phenomena, and therefore the resulting process. To progress to new advanced applications for LSP and CP, evaluation and validation of the process uniformity over geometric features is therefore crucial. Some of the reported results in the present work clearly reveal that for different geometries, the strain uniformity can be poor which would of course compromise potential performance enhancement. Existing techniques to confirm application of uniform compressive strains make this challenging, which can potentially be addressed by Bragg edge strain imaging. The strain maps can also be used to inform the optimum peening parameters to obtain maximum compressive surface stress without reverse yielding and can also

indicate the location and magnitude of the balancing tensile stress. For example, the balancing in-plane tensile residual strain can be observed on the AA7050 samples, especially those on which high peening coverage was applied, i.e., S10 and S20. The results from Bragg edge imaging can be correlated and complemented with data from other tests such as fatigue crack initiation and growth. Bragg edge imaging can provide other useful information such as plasticity, demonstrated by the plastic deformation region due to very high peening coverage, In Fig. 8(c).

6. Conclusions

Examples of the use of Bragg edge radiography for near-surface residual strain mapping have been presented, particularly for the application of mechanical surface treatment research. From these exercises, some conclusion can be drawn as follows:

The wealth of information provided by the strain maps emphasises the advantage of Bragg edge neutron transmission for strain mapping over diffraction-based methods. Most neutron strain scanners are limited by size of available gauge volumes to resolve a high strain gradient that is often present within the first few hundred microns. Partially filled gauge volume effects will also be an issue for residual strain measurement at sample surfaces. Synchrotron X-ray diffraction might have sufficient spatial resolution to measure strain in selected components, but it requires hundreds to thousands of measurement points in order to obtain an overall coverage of a sample, and residual strain profiles within complex-shaped features. Additionally, positioning accuracies of the measurement might present a problem for the two aforementioned technique, although a procedure to manage the alignment has been presented elsewhere [57]. Despite only providing through-thickness averaged strain information in one direction, Bragg edge neutron transmission can quickly and straightforwardly determine a multitude of strain profiles. This can help identify regions of interest in the sample, should a full stress measurement using any other methods be required.

Strain maps produced by Bragg edge imaging show good agreement with the results from the more established methods, i.e., X-ray diffraction and neutron diffraction. Thus, strains obtained by Bragg edge neutron radiography can be considered accurate and representative of the residual stress state of the sample for slowly varying strain profiles. However, it is clear that the spatial resolution limits of the Bragg edge methods need to be considered when interpreting strain values, in order to avoid misinterpretation of averaged, unresolved strain curves.

While the higher transmission under the laser peened region was previously thought as the contribution of crystallographic texture change, it was proven that this was rather the effect of considerable shifts in the position (thus strain) of intense Bragg edges. Therefore, for analysis of energy selective radiographs one should be mindful of coexisting structural properties of texture, phase, and strain in a sample, as shown by the presented examples.

This study has shown that strain information can still be extracted from a highly textured sample. That said, further investigation is still required to determine whether a change in texture, which changes the height and/or shape of Bragg edges, may introduce false strain reading (pseudo-strain). Among the possibilities to separate strain from the texture effects is sample annealing at temperatures, where residual strain is relaxed while texture remains unaffected. Consequently, the annealed sample can be used for the determination of stress-free lattice parameters (spatially resolved across the sample), thus allowing separation of measured strain from texture related effects.

Declaration of Competing Interest

The authors declare that they have no known competing financial interests or personal relationships that could have appeared to influence the work reported in this paper.

Acknowledgments

RSR would like to acknowledge STFC for their support through the sponsored PhD program under ISIS facility development studentship. The authors are grateful for beam time provision on IMAT, ISIS, UK (10.5286/ISIS.E.RB1820631; 10.5286/ISIS.E.RB1910464), RADEN, MLF, Japan (Proposal No. 2018A0155), and SALSA, ILL, France (10.5291/ILL-DATA.1-02-315). This research was partly supported by JSPS KAKENHI, grant numbers 18KK0103 and 20H02021. MEF is grateful for funding from the Lloyd's Register Foundation, a charitable foundation helping to protect life and property by supporting engineering- related education, public engagement and the application of research.

References

[1] Y.S. Nam, Y.I. Jeong, B.C. Shin, J.H. Byun, Enhancing surface layer properties of an aircraft aluminum alloy by shot peening using response surface methodology, Mater. Des. 83 (2015) 566–576, doi:10.1016/j.matdes.2015.06.065.
[2] Y.K. Gao, X.R. Wu, Experimental investigation and fatigue life prediction for 7475-T7351 aluminum alloy with and without shot peening-induced residual stresses, Acta Materialia 59 (2011) 3737–3747, doi:10.1016/j.actamat.2011.03.013.
[3] M. Dorman, M.B. Toparli, N. Smyth, A. Cini, M.E. Fitzpatrick, P.E. Irving, Effect of laser shock peening on residual stress and fatigue life of clad 2024 aluminium sheet containing scribe defects, Mater. Sci. Eng. A 548 (2012) 142–151, doi:10.1016/j.msea.2012.04.002.
[4] T. Kostilnik, Shot peening, in: Surface Engineering, ASM International, 1994, pp. 126–135, doi:10.31399/asm.hb.v05.a0001235.
[5] C.S. Montross, T. Wei, L. Ye, G. Clark, Y.W. Mai, Laser shock processing and its effects on microstructure and properties of metal alloys: a review, Int. J. Fatigue 24 (2002) 1021–1036, doi:10.1016/S0142-1123(02)00022-1.
[6] H. Soyama, Cavitation peening: a review, Metals 10 (2020) (Basel), doi:10.3390/met10020270.
[7] M.R. Hill, The slitting method, in: Practical Residual Stress Measurement Methods, John Wiley & Sons, 2013, pp. 89–108, doi:10.1002/9781118402832.ch4.
[8] ASTM. E837-13a, Standard Test Method for Determining Residual Stresses by the Hole-Drilling Strain-Gage Method, ASTM International, West Conshohocken, PA, 2013, doi:10.1520/E0837-13A.
[9] B.B. He, U. Preckwinkel, S. Kingsley, Advantages of using 2D detectors for residual stress measurements, Advances in X-ray Analysis 42 (1998) 429–438.
[10] E. Maawad, Y. Sano, L. Wagner, H.G. Brokmeier, C. Genzel, Investigation of laser shock peening effects on residual stress state and fatigue performance of titanium alloys, Mater. Sci. Eng. A 536 (2012) 82–91, doi:10.1016/j.msea.2011.12.072.
[11] C. Polese, D. Glaser, M. Newby, Synchrotron XRD evaluation of residual stresses introduced by laser shock peening for steam turbine blade applications, Mater. Res. Proc. 4 (2018) 97–102, doi:10.21741/9781945291678-15.
[12] M.B. Toparli, M.E. Fitzpatrick, Residual stresses induced by laser peening of thin aluminium plates, Mater. Sci. Forum 681 (2011) 504–509, doi:10.4028/www.scientific.net/MSF.681.504.
[13] M. Achintha, D. Nowell, K. Shapiro, P.J. Withers, Eigenstrain modelling of residual stress generated by arrays of laser shock peening shots and determination of the complete stress field using limited strain measurements, Surf. Coat. Technol. 216 (2013) 68–77, doi:10.1016/j.surfcoat.2012.11.027.
[14] M. Pavan, D. Furfari, B. Ahmad, M.A. Gharghouri, M.E. Fitzpatrick, Fatigue crack growth in a laser shock peened residual stress field, Int. J. Fatigue 123 (2019) 157–167, doi:10.1016/j.ijfatigue.2019.01.020.
[15] D. Glaser, M. Newby, C. Polese, L. Berthe, A.M. Venter, D. Marais, J.P. Nobre, G. Styger, S. Paddea, S.N. van Staden, Evaluation of residual stresses introduced by laser shock peening in steel using different measurement techniques, in: Mechanical Stress Evaluation by Neutrons and Synchrotron Radiation, 4, Materials Research Proceedings, 2018, pp. 45–50, doi:10.21741/9781945291678-7.
[16] J.R. Santisteban, L. Edwards, M.E. Fitzpatrick, A. Steuwer, P.J. Withers, M.R. Daymond, M.W. Johnson, N. Rhodes, E.M. Schooneveld, Strain imaging by Bragg edge neutron transmission, Nucl. Instrum. Methods Phys. Res. Sect. A Accel. Spectrom. Detect. Assoc. Equip. 481 (2002) 765–768, doi:10.1016/S0168-9002(01)01256-6.
[17] K. Iwase, H. Sato, S. Harjo, T. Kamiyama, T. Ito, S. Takata, K. Aizawa, Y. Kiyanagi, In situ lattice strain mapping during tensile loading using the neutron trans-

mission and diffraction methods, J. Appl. Crystallogr. 45 (2012) 113–118, doi:10.1107/S0021889812000076.
[18] A.S. Tremsin, T.Y. Yau, W. Kockelmann, Non-destructive examination of loads in regular and self-locking spiralock ® threads through energy- resolved neutron imaging, Strain 52 (2016) 548–558, doi:10.1111/str.12201.
[19] R.S. Ramadhan, A.K. Syed, A.S. Tremsin, W. Kockelmann, R. Dalgliesh, B. Chen, D. Parfitt, M.E. Fitzpatrick, Mapping residual strain induced by cold working and by laser shock peening using neutron transmission spectroscopy, Mater. Des. 143 (2018), doi:10.1016/j.matdes.2018.01.054.
[20] R.S. Ramadhan, W. Kockelmann, T. Minniti, B. Chen, D. Parfitt, M.E. Fitzpatrick, A.S. Tremsin, Characterization and application of Bragg-edge transmission imaging for strain measurement and crystallographic analysis on the IMAT beamline, J. Appl. Crystallogr. 52 (2019) 351–368, doi:10.1107/S1600576719001730.
[21] M. Morgano, N. Kalentics, C. Carminati, J. Capek, M. Makowska, R. Woracek, T. Maimaitiyili, T. Shinohara, R. Loge, M. Strobl, Investigation of the effect of laser shock peening in additively manufactured samples through Bragg edge neutron imaging, Addit. Manuf. 34 (2020) 101201, doi:10.1016/j.addma.2020.101201.
[22] R. Woracek, J. Santisteban, A. Fedrigo, M. Strobl, Diffraction in neutron imaging—A review, Nucl. Instrum. Methods Phys. Res. Sect. A Accel. Spectrom. Detect. Assoc. Equip. 878 (2018) 141–158, doi:10.1016/j.nima.2017.07.040.
[23] W. Kockelmann, G. Frei, E.H. Lehmann, P. Vontobel, J.R. Santisteban, Energy-selective neutron transmission imaging at a pulsed source, Nucl. Instrum. Methods Phys. Res. Sect. A Accel. Spectrom. Detect. Assoc. Equip. 578 (2007) 421–434, doi:10.1016/j.nima.2007.05.207.
[24] A.S. Tremsin, J.V. Vallerga, J.B. McPhate, O.H.W. Siegmund, R. Raffanti, High resolution photon counting with MCP-timepix quad parallel readout operating at >1 KHz frame rates, IEEE Trans. Nucl. Sci. 60 (2013) 578–585, doi:10.1109/TNS.2012.2223714.
[25] T. Shinohara, T. Kai, K. Oikawa, T. Nakatani, M. Segawa, K. Hiroi, Y. Su, M. Ooi, M. Harada, H. Iikura, H. Hayashida, J.D. Parker, Y. Matsumoto, T. Kamiyama, H. Sato, Y. Kiyanagi, The energy-resolved neutron imaging system, RADEN, Rev. Sci. Instrum. (2020) 91, doi:10.1063/1.5136034.
[26] W. Kockelmann, T. Minniti, R. Ramadhan, R. Ziesche, D.E. Pooley, S.C. Capelli, D. Glaser, A.S. Tremsin, Wavelength-resolved neutron imaging on IMAT, Neutron Radiogr. 15 (2020) 29–34 WCNR-11, doi:10.21741/9781644900574-5.
[27] T. Pirling, Precise analysis of near surface neutron strain imaging measurements, Procedia Eng. 10 (2011) 2147–2152, doi:10.1016/j.proeng.2011.04.355.
[28] S. Vogel, A Rietveld-Approach for the Analysis of Neutron Time-Of-Flight Transmission Data, Christian-Albrechts-Universität zu Kiel, 2000.
[29] A.W.T. Gregg, J.N. Hendriks, C.M. Wensrich, A. Wills, A.S. Tremsin, V. Luzin, T. Shinohara, O. Kirstein, M.H. Meylan, E.H. Kisi, Tomographic reconstruction of two-dimensional residual strain fields from Bragg-edge neutron imaging, Phys. Rev. Appl. 10 (2018) 1, doi:10.1103/PhysRevApplied.10.064034.
[30] T. Minniti, K. Watanabe, G. Burca, D.E. Pooley, W. Kockelmann, Characterization of the new neutron imaging and materials science facility IMAT, Nucl. Instrum. Methods Phys. Res. 888 (2018) 184–195, doi:10.1016/j.nima.2018.01.037.
[31] J.R. Santisteban, L. Edwards, A. Steuwer, P.J. Withers, Time-of-flight neutron transmission diffraction, J. Appl. Crystallogr. 34 (2001) 289–297, doi:10.1107/S0021889801003260.
[32] A. Steuwer, P.J. Withers, J.R. Santisteban, L. Edwards, G. Bruno, M.E. Fitzpatrick, M.R. Daymond, M.W. Johnson, D. Wang, Bragg edge determination for accurate lattice parameter and elastic strain measurement, Phys. Status Solidi 185 (2001) 221–230 Appl. Res.2<221::AID−PSSA221>3.0.CO;2-C, doi:10.1002/1521-396X(200106)185.
[33] A.S. Tremsin, J.B. McPhate, W.A. Kockelmann, J.V. Vallerga, O.H.W. Siegmund, W.B. Feller, Energy-Resolving neutron transmission radiography at the ISIS pulsed spallation source with a high-resolution neutron counting detector, IEEE Trans. Nucl. Sci. 56 (2009) 2931–2937, doi:10.1109/TNS.2009.2029690.
[34] H. Sato, T. Kamiyama, Y. Kiyanagi, A rietveld-type analysis code for pulsed neutron Bragg-edge transmission imaging and quantitative evaluation of texture and microstructure of a welded alpha-iron plate, Mater. Trans. 52 (2011) 1294–1302, doi:10.2320/Matertrans.M2010328.
[35] J.N. Hendriks, A.W.T. Gregg, R.R. Jackson, C.M. Wensrich, A. Wills, A.S. Tremsin, T. Shinohara, V. Luzin, O. Kirstein, Tomographic reconstruction of triaxial strain fields from Bragg-edge neutron imaging, Phys. Rev. Mater. 3 (2019) 1–11, doi:10.1103/PhysRevMaterials.3.113803.
[36] H. Sato, Y. Shiota, T. Shinohara, T. Kamiyama, M. Ohnuma, M. Furusaka, Y. Kiyanagi, Development of the tensor CT algorithm for strain tomography using Bragg-edge neutron transmission, Phys. Procedia 69 (2015) 349–357, doi:10.1016/j.phpro.2015.07.049.
[37] B. Abbey, S.Y. Zhang, W. Vorster, A.M. Korsunsky, Reconstruction of axisymmetric strain distributions via neutron strain tomography, Nucl. Instrum. Methods Phys. Res. Sect. B Beam Interact. Mater. At. 270 (2012) 28–35, doi:10.1016/j.nimb.2011.09.012.
[38] W.R.B. Lionheart, P.J. Withers, Diffraction tomography of strain, Inverse Probl. 31 (2015) 045005, doi:10.1088/0266-5611/31/4/045005.
[39] W. Kockelmann, T. Minniti, D. Pooley, G. Burca, R. Ramadhan, F. Akeroyd, G. Howells, C. Moreton-Smith, D. Keymer, J. Kelleher, S. Kabra, T. Lee, R. Ziesche, A. Reid, G. Vitucci, G. Gorini, D. Micieli, R. Agostino, V. Formoso, F. Aliotta, R. Ponterio, S. Trusso, G. Salvato, C. Vasi, F. Grazzi, K. Watanabe, J. Lee, A. Tremsin, J. McPhate, D. Nixon, N. Draper, W. Halcrow, J. Nightingale, Time-of-flight neutron imaging on IMAT@ISIS: a new user facility for materials science, J. Imaging 4 (2018) 47, doi:10.3390/jimaging4030047.
[40] A. Naito, O. Takakuwa, H. Soyama, Development of peening technique using recirculating shot accelerated by water jet, Mater. Sci. Technol. (2012), doi:10.1179/174328471lY.0000000027.
[41] T. Abbasi, S.A. Abbasi, Dust explosions-Cases, causes, consequences, and control, J. Hazard. Mater. (2007), doi:10.1016/j.jhazmat.2006.11.007.
[42] H. Soyama, Comparison of various XRD methods on evaluation of residual stress introduced by submerged laser peening, Met. Finish. News 19 (2018) 54–57.
[43] N. Saitou, K. Enomoto, K. Kurosawa, M. Tanaka, R. Morinaka, F. Yoshikubo, T. Ishikawa, H. Yano, Development of water jet peening technique for reactor internals of nuclear power plant, in: Proceedings of the 1992 Annual Meeting of JSME/MMD, 2004, doi:10.1299/jsmezairiki.2004.0_205.
[44] H. Soyama, D. Sanders, Use of an abrasive water cavitating jet and peening process to improve the fatigue strength of titanium alloy 6Al-4V manufactured by the electron beam powder bed melting (EBPB) additive manufacturing method, JOM (2019), doi:10.1007/s11837-019-03673-8.
[45] H. Soyama, K. Sasaki, D. Odhiambo, M. Saka, Cavitation shotless peening for surface modification of alloy tool steel, JSME Int. J. Ser. A (2003) Solid Mech. Mater. Eng., doi:10.1299/jsmea.46.398.
[46] R. Specht, F. Harris, L. Lane, D. Jones, L. Hackel, T. Zaleski, J. Halpin, M. Hill, W. Wübbenhorst, Process control techniques for laser peening of metals, in: Shot Peening, John Wiley & Sons, Ltd, 2003, pp. 474–482, doi:10.1002/3527606580.ch61.
[47] T. Pirling, G. Bruno, P.J. Withers, SALSA: advances in residual stress measurement at ILL, Mater. Sci. Forum 524–525 (2006) 217–222, doi:10.4028/www.scientific.net/msf.524-525.217.
[48] T. Pirling, D.J. Hughes, J.S. Robinson, Precise determination of residual stresses in large specimens by neutron diffraction, in: Mechanical Stress Evaluation by Neutrons and Synchrotron Radiation, Trans Tech Publications Ltd, 2010, pp. 80–85, doi:10.4028/www.scientific.net/MSF.652.80.
[49] A.S. Tremsin, S. Ganguly, S.M. Meco, G.R. Pardal, T. Shinohara, W.B. Feller, Investigation of dissimilar metal welds by energy-resolved neutron imaging, J. Appl. Crystallogr. 49 (2016) 1130–1140, doi:10.1107/S1600576716006725.
[50] J. Schindelin, I. Arganda-Carreras, E. Frise, V. Kaynig, M. Longair, T. Pietzsch, S. Preibisch, C. Rueden, S. Saalfeld, B. Schmid, J.Y. Tinevez, D.J. White, V. Hartenstein, K. Eliceiri, P. Tomancak, A. Cardona, Fiji: an open-source platform for biological-image analysis, Nat. Methods 9 (2012) 676–682, doi:10.1038/nmeth.2019.
[51] H. Soyama, A. Lichtarowicz, T. Momma, E.J. Williams, A new calibration method for dynamically loaded transducers and its application to cavitation impact measurement, J. Fluids Eng. Trans. ASME (1998), doi:10.1115/1.2820728.
[52] T. Okada, S. Hattori, M. Shimizu, A fundamental study of cavitation erosion using a magnesium oxide single crystal (intensity and distribution of bubble collapse impact loads), Wear (1995), doi:10.1016/0043-1648(95)07162-8.
[53] A. Reid, I. Martinez, M. Marshall, T. Minniti, S. Kabra, W. Kockelmann, T. Connolley, M. Mostafavi, Mapping of axial plastic zone for roller bearing overloads using neutron transmission imaging, Mater. Des. 156 (2018) 103–112, doi:10.1016/j.matdes.2018.06.042.
[54] H. Sato, T. Sato, Y. Shiota, T. Kamiyama, A.S. Tremsin, M. Ohnuma, Y. Kiyanagi, Relation between Vickers hardness and Bragg-edge broadening in quenched steel rods observed by pulsed neutron transmission imaging, Mater. Trans. 56 (2015) 1147–1152, doi:10.2320/matertrans.M2015049.
[55] H. Soyama, Improvement of fatigue characteristics of welded parts by cavitation peening, Journal of the Japan Welding Society 91 (2022) 195–199.
[56] D. Glaser, C. Polese, R.D. Bedekar, J. Plaisier, S. Pityana, B. Masina, T. Mathebula, E. Troiani, Laser shock peening on a 6056-T4 aluminium alloy for airframe applications, Adv. Mater. Res. 891–892 (2014) 974–979, doi:10.4028/www.scientific.net/AMR.891-892.974.
[57] R.S. Ramadhan, S. Cabeza, T. Pirling, S. Kabra, M. Hofmann, J. Rebelo Kornmeier, A.M. Venter, D. Marais, Quantitative analysis and benchmarking of positional accuracies of neutron strain scanners, Nucl. Instrum. Methods Phys. Res. Sect. A Accel. Spectrom. Detect. Assoc. Equip. 999 (2021) 165230, doi:10.1016/j.nima.2021.165230.